Thermal evidence for Taylor columns in turbulent rotating Rayleigh-Bénard convection

Eric M. King and Jonathan M. Aurnou

Phys. Rev. E **85**, 016313 — Published 18 January 2012

DOI: 10.1103/PhysRevE.85.016313

Thermal evidence for Taylor columns in turbulent, rotating Rayleigh-Bénard convection

Eric M. King

Department of Earth and Planetary Science,

University of California, Berkeley, 94720 USA

Jonathan M. Aurnou

Department of Earth and Space Sciences,

University of California, Los Angeles, 90095-1567 USA

Abstract

We investigate flow structures in rotating Rayleigh-Bénard convection experiments in water using thermal measurements. We focus on correlations between time series measurements of temperature in the top and bottom boundaries. Distinct anti-correlations are observed for rapidly rotating convection, which are argued to attest to heat transport by convective Taylor columns. In support of this argument, these quasi-geostrophic flow structures are directly observed in flow visualizations, and their thermal signature is qualitatively reproduced by a simple model of heat transport by columnar flow. Weakly– and non–rotating convection produces positively correlated temperature changes across the layer, indicative of heat transport by large scale circulation. We separate these regimes using a transition parameter that depends on the Rayleigh and Ekman numbers, $RaE^{3/2}$.

I. INTRODUCTION

Fluid motions in planetary systems are subject to Coriolis forces resulting from the planet's rotation. A strong Coriolis force imposes an organizational influence on otherwise turbulent flow that is thought to be responsible for, *inter alia*, the alignment of Earth's rotation axis and magnetic dipole. Here, we examine results from a simple experimental analog of such planetary fluid systems: rotating Rayleigh-Bénard convection.

Rayleigh-Bénard convection (RBC) is a horizontal layer of fluid through which heat is fluxed from bottom to top. Fluid near the bottom boundary is warmed, expands, and rises due to gravitational instability. Rotating RBC has an identical setup, but fluid and boundaries spin about a vertical axis. Many planetary convection systems are considered rapidly rotating, meaning that the period of rotation is among the fastest dynamical timescales present. Rapidly rotating flows are typically described by the so–called geostrophic force balance, a balance between the Coriolis force and pressure gradient. The curl of this force balance produces the Taylor–Proudman theorem [1]:

$$\Omega\hat{\mathbf{z}} \cdot \boldsymbol{\nabla}\mathbf{u} = 0; \tag{1}$$

where $\Omega\hat{\mathbf{z}}$ and $\mathbf{u}$ are the rotation and flow vectors, respectively. Although convective flow cannot strictly abide by this constraint beyond the lowest order, a strong Coriolis force nevertheless tends to align flow with the axis of rotation in what is considered quasi-geostrophic convection

Flow in quasi-geostrophic RBC is manifest as a vortex grid of so-called convective Taylor columns (CTCs) [e.g., 2]. A CTC is a helical vortex with either upward or downward flow [3]. The sign of vorticity ($\boldsymbol{\omega} \equiv \boldsymbol{\nabla} \times \mathbf{u}$) in an upward flowing CTC is positive in the lower half of the layer ($z < h/2$), and negative in the upper half ($z > h/2$). Conversely, a downward flowing CTC will have negative vorticity in the lower half of the layer, and positive vorticity in the upper half. For both upward and downward flowing CTCs, then, helicity ($\mathbf{u} \cdot \boldsymbol{\omega}$) is positive in the lower half and negative in the upper half. A schematic depiction of CTCs is shown in figure 1a.

For rapidly rotating convection, roughly equal numbers of upward and downward flowing CTCs are expected [4]. Vortex-vortex interactions between the CTCs cause them to be advected laterally about the container [e.g., 5]. This horizontal 'dance' of the axial CTCs

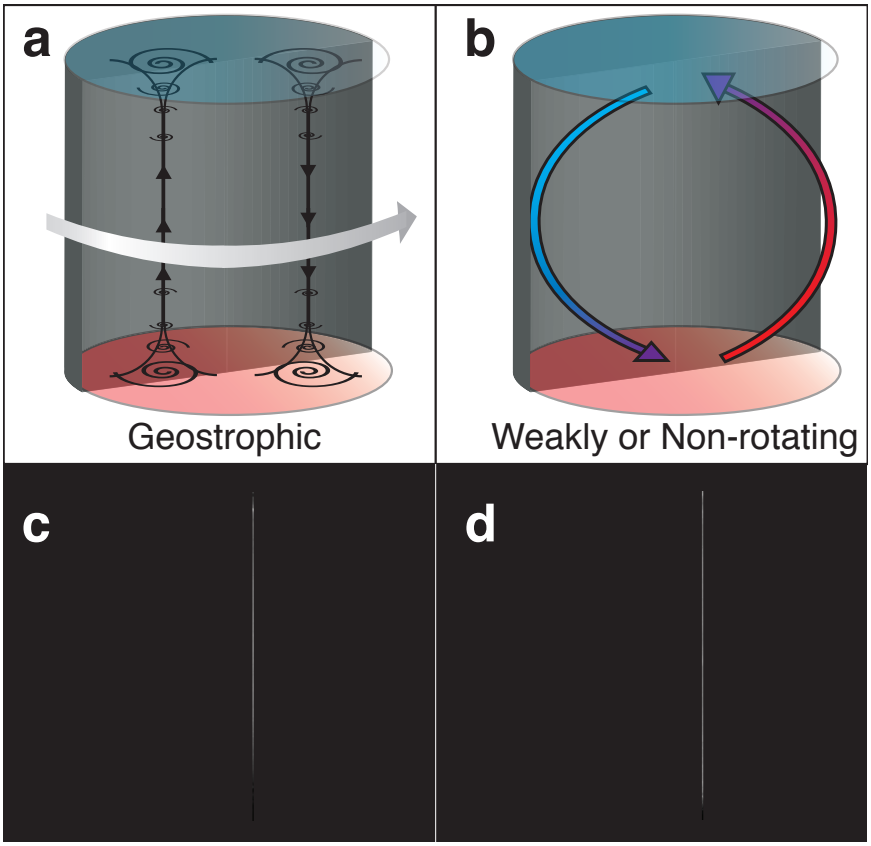

FIG. 1: Flow regimes in rotating RBC. **a)** An illustration of two convective Taylor columns (CTCs) in quasi-geostrophic convection. **b)** An illustration of a large scale circulation typical of turbulent weakly or non-rotating RBC. **c** & **d)** Visualizations of flow regimes in rotating RBC experiments. A vertical sheet of laser light is projected through the center of a 20 cm tall, uninsulated convection tank. Both panels show convection in water (plus trace amounts of Kalliroscope particles) driven by 100 W of heating power and rotated at 4.3 Hz (panel c) and 0.43 Hz (panel d). Approximate non-dimensional parameters are then: $Pr \approx 7$; $R_f \approx 1.1 \times 10^{11}$; $E \approx 3 \times 10^{-6}$ (panel c) and $E \approx 3 \times 10^{-5}$ (panel d).

has been observed in movies of quasi-geostrophic RBC in experiments [6] and numerical simulations [4, 7].

If a convection system rotates slowly enough or if the vigor of convection is strong enough, inertial forces can overwhelm the Coriolis force, resulting in weakly rotating convection, which behaves similarly to non-rotating convection. Experimental work [e.g., 8, 9] has seen the development of large scale circulation in weakly rotating convection like those typical

of non-rotating RBC experiments [e.g., 10, 11]. This large scale circulation results from the interaction of non-linear entrainment processes and the experimental convection tank geometry [12]. Figure 1b shows a schematic depiction of the flywheel pattern of a large scale circulation.

The different regimes of rotating convection are often examined using heat transfer measurements in experiments and simulations to distinguish competing influences of buoyancy and rotation [e.g., 7, 13–20]. Some work, however, is able to connect flow and heat transfer regimes. Refs. [21, 22], for example, measure heat transfer efficiency and helicity in rotating RBC simulations, showing that heat transfer and flow structure regimes are linked by a relationship that depends only on the Prandtl number. Experimentally, it is difficult to simultaneously characterize flow patterns and heat transfer, as visualization techniques can compromise thermal control [e.g., 23]. Here, we measure temporal correlations of thermal signals to infer large scale patterns of convection in rotating RBC experiments. For quasi-geostrophic convection, in particular, we may expect that the random horizontal dance of the CTCs should produce significant thermal anomalies nearly simultaneously on stationary, vertically aligned temperature probes.

II. METHOD

A. Experiments

We conduct rotating convection experiments in water ($Pr \approx 7$) and sucrose solution ($Pr \approx 10$) using the rotating magnetoconvection device at UCLA. Figure 2 shows a schematic depiction of the experimental setup. The convection tank is a 20 cm diameter cylinder whose top and bottom endwalls are 4 cm thick aluminum and 1.3 cm thick copper blocks, respectively. The fluid is contained by polycarbonate sidewalls with heights varying between 3.2 cm and 19.7 cm. An electrical heating element is mechanically fixed to the bottom of the lower endwall. Between 5 and 600 Watts of heat is passed through the endwalls and fluid, and is removed above the upper endwall by thermostated water flowing through an aluminum heat exchanger, which is isothermal to within 0.05 K. The convection tank setup is insulated by closed cell foam, 20 cm thick, to minimize heat losses through the sidewalls. The experimental apparatus (convection tank setup and diagnostic systems) is

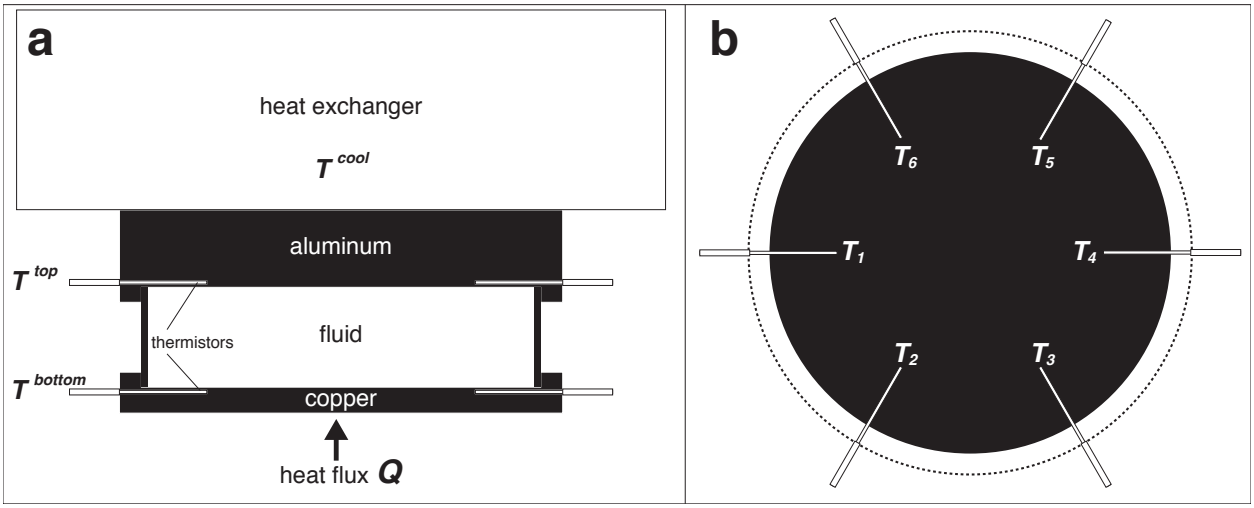

FIG. 2: A scaled illustration of the experimental apparatus. **a)** A sideview showing the vertical structure of the tank setup with a 5 cm sidewall. $T^{\rm top}$ and $T^{\rm bottom}$ show the vertical locations of the top and bottom thermistors. **b)** A plan view of the convection tank setup showing the horizontal orientation of the top and bottom thermistor pairs, $T_{1,\ldots,6}$.

rotated up to fifty revolutions per minute (5.2 Hz). More detailed descriptions of the device and experimental method can be found in refs. [24, 25].

We report results from a suite of 64 rotating and 12 non-rotating convection experiments. These experiments represent a subset of those presented in [7, 25]. Time series from each experiment have at least 25,000 data points, acquired at 10 Hz for at least 45 minutes. The control parameters fixed experimentally are tank height, h, rotation rate, Ω, input heat power Q, as well as fluid properties. The non-dimensional parameters fixed for each convection experiment are the Prandtl number, Pr, Ekman number, E, flux Rayleigh number, R_f, and the tank diameter-to-height aspect ratio, Γ. Table I defines these and other relevant experimental parameters. In this study, we focus on changes in dynamics as R_f and E vary over several orders of magnitude.

Figure 1 (c & d) shows frames from video taken in a complementary set of experiments for qualitative visualization. Here, the insulation is removed from the sidewall of the convection tank, and Kalliroscope particles in water are illuminated by a vertical sheet of laser light projected through the center of the tank [e.g., 26]. Such visualizations allow us to check more directly the existence of CTCs that are indirectly observed using temperature time

Parameter	Definition	Experiments
	Dimensional	
h	tank height	$0.032\ \text{m} \leq h \leq 0.197\ \text{m}$
Q	heat power	$5\ \text{W} \leq Q \leq 600\ \text{W}$
Ω	rotation rate	$0\ \text{Hz} \leq \Omega \leq 5.2\ \text{Hz}$
ν	viscous diffusivity	$7.2 \times 10^{-7}\ \text{m}^2/\text{s} \leq \nu \leq 1.5 \times 10^{-6}\ \text{m}^2/\text{s}$
κ	thermal diffusivity	$1.4 \times 10^{-5}\ \text{m}^2/\text{s}$
α_T	thermal expansivity	$0.002\ \text{K}^{-1} \leq \alpha_T \leq 0.0043\ \text{K}^{-1}$
k	thermal conductivity	0.6 W/mK
A	cross-sectional area	$0.0314\ \text{m}^2$
ΔT	temperature difference	$2.2\ \text{K} \leq \Delta T \leq 45\ \text{K}$
	Dimensionless	
Aspect Ratio	$\Gamma \equiv (4A/(\pi h^2))^{1/2}$	$1 \leq \Gamma \leq 6.2$
Prandtl number	$Pr \equiv \nu/\kappa$	$4.8 \lesssim Pr \lesssim 11$
Ekman number	$E \equiv \nu/(2\Omega h^2)$	$2.5 \times 10^{-6} \lesssim E \lesssim \infty$
flux Rayleigh number	$R_f \equiv (\alpha_T g Q h^4)/(A\nu\kappa k)$	$8.8 \times 10^6 \lesssim R_f \lesssim 5.3 \times 10^{11}$
Rayleigh number	$Ra \equiv (\alpha_T g \Delta T h^3)/(\nu\kappa)$	$10^6 \lesssim Ra \lesssim 5.5 \times 10^9$
Nusselt number	$Nu \equiv (Qh)/(Ak\Delta T)$	$6.2 \lesssim Nu \lesssim 96.2$

TABLE I: Relevant experimental parameters.

series measurements in thermally insulated experiments.

The prime diagnostic of interest here is temperature time series measurements. We use these measurements to distinguish the two flow regimes depicted in figure 1. To accomplish this goal, we place six thermistors within the solid bottom endwall, 2 mm below the fluid, and another six thermistors within the solid top endwall, 2 mm above the fluid (see figure 2a). The probes are arranged to form six vertically aligned pairs, equally spaced in azimuth (see

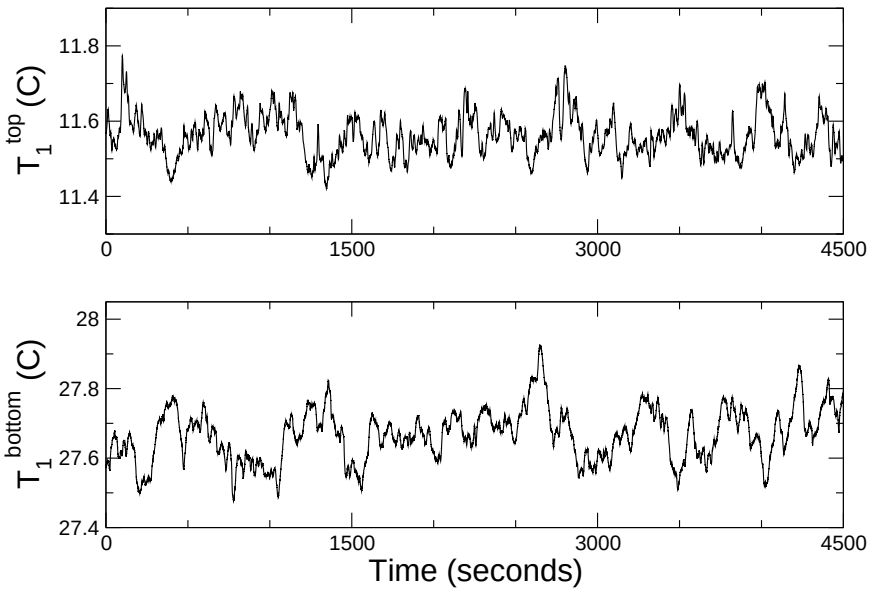

FIG. 3: An example of temperature time series data from a rotating RBC experiment ($R_f = 1.1 \times 10^{11}, E = 3 \times 10^{-6}$). The top panel shows measurements from a single thermistor in the top endwall ($T_1^{\rm top}(t)$), and the bottom panel shows measurements from a thermistor below the fluid ($T_1^{\rm bottom}(t)$).

figure 2b). Figure 3 shows an example of temperature time series measurements from a thermistor within each of the top and bottom endwalls. These temperature measurements are denoted $T_i^{\rm top}(t)$ and $T_i^{\rm bottom}(t)$, where $i = 1, ..., 6$, corresponding to azimuthal location (see figure 2b). The temperature cross-correlation is calculated using temperature time series measurements of top and bottom thermistors at the same location in azimuth:

$$C_i^{\rm top-bottom}(m) = \sum_{t/dt=0}^{N-|m|-1} \left(T_i^{\rm top}(t) - \left\langle T_i^{\rm top}(t)\right\rangle_t\right)\left(T_i^{\rm bottom}(t+m\,dt) - \left\langle T_i^{\rm bottom}(t)\right\rangle_t\right); \quad (2)$$

where t is the measurement time and dt is the inverse of the data acquisition frequency such that $t/dt = 0, 1, ..., N$, where N is the total number of data points acquired in time, and integers $m = 1-2N, ..., 2N-1$ represent the correlation lag. $C_i(m)$ is then normalized such that the auto-correlation at zero lag, $C_i^{\rm top-top}(m=0)$, is unity.

The mean, zero-lag correlation of the six pairs can be calculated such that a single

correlation coefficient is produced for each convection experiment:

$$\overline{C} = \sum_{i=1}^{6} C_i^{\text{top-bottom}}(m = 0). \tag{3}$$

This quantity allows us to gauge the nature of flow structures as a function of our changing parameters for all 76 experiments conducted.

III. RESULTS

Figure 1 shows visualizations of quasi-geostrophic (panel c) and weakly rotating (panel d) convection in uninsulated experiments. We quantify the relative influence of rotation and buoyancy using the transition parameter of ref. [25]. The transition between quasi-geostrophic and weakly rotating convection regimes is argued to be controlled by the relative thicknesses of the thermal and Ekman boundary layers [7], and the ratio of their thicknesses can be characterized by a transition parameter $RaE^{3/2}$. We show in [25] that the thermal boundary layer becomes thinner than the Ekman boundary layers when $RaE^{3/2} \gtrsim 20$, which coincides with a transition from quasi-geostrophic to weakly rotating heat transfer behavior. The quasi-geostrophic experiment shown in figure 1c has $RaE^{3/2} \approx 8$, and the weakly rotating experiment shown in panel d has $RaE^{3/2} \approx 280$. The former experiment reveals the existence of container-high CTCs in the more rapidly rotating case (c), but, in order to expose the fluid for visualization, are not well controlled thermally.

Figure 4 **a** and **b** show measurements of $C_i^{\text{top-bottom}}$ from quasi-geostrophic convection experiments for each of the six thermistor pairs ($i = 1, ..., 6$). Panel a has $R_f = 2 \times 10^8$, and $E = 4.4 \times 10^{-5}$. Panel b has $R_f = 1.1 \times 10^{11}$, and $E = 3 \times 10^{-6}$ (identical to the experiments shown in figure 1c). These convection experiments are considered quasi-geostrophic, as they have $RaE^{3/2} \approx 5$ and $RaE^{3/2} \approx 8$, respectively, and transport heat less efficiently than non-rotating, but otherwise identical experiments (by 30% and 10%, respectively). The instantaneous ($m = 0$) thermal variations are vertically anti-correlated.

The *anti*-correlation of these quasi-geostrophic temperature signals is perhaps counterintuitive. Upward flowing CTCs transport warm material from bottom boundary to top, and downward flowing columns bring cold material from top to bottom. The CTCs are then either anomalously hot or cold, and measurements of temperature on vertical pairs of thermistors within the fluid should exhibit positive correlations. Our measurements, however,

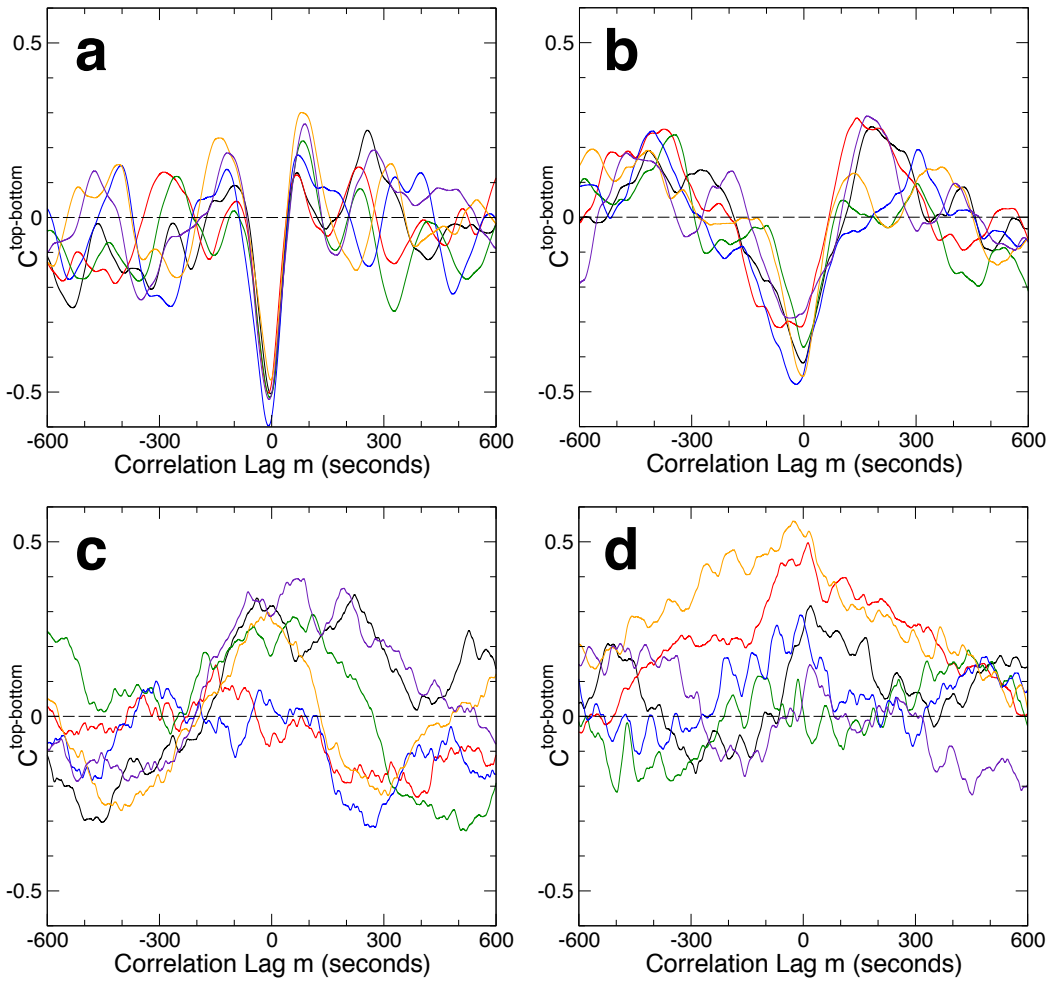

FIG. 4: Temperature correlations from vertical thermistor pairs, $C_i^{\text{top-bottom}}$, versus correlation lag, $m \times dt$, as defined in (3). Case a has $h = 4.7$ cm and $Q = 50$ W, and therefore $R_f = 2 \times 10^8$. Cases b-d have $h = 0.197$ m and $Q = 100$ W, and therefore $R_f = 1.1 \times 10^{11}$. **a)** Rotating convection with $\Omega = 5.3$ Hz, $E = 4.4 \times 10^{-5}$, $RaE^{3/2} \approx 5$. **b)** Rotating convection with $\Omega = 4.3$ Hz, $E = 3 \times 10^{-6}$, $RaE^{3/2} \approx 8$. **c)** Rotating convection with $\Omega = 0.43$ Hz, $E = 3 \times 10^{-5}$, $RaE^{3/2} \approx 280$. **d)** Non-rotating convection.

are taken in the tank's endwall, not in the fluid, and this difference is important in producing the anticorrelated thermal signals. Convective heat transfer can be parameterized locally as $\mathbf{u}T'$, where T' is the local temperature anomaly [e.g., 27]. Both warm, upward flowing, and cold, downward flowing CTCs transport heat upward. Vertical conduits of heat such as CTCs will simultaneously cool the bottom boundary and warm the top boundary.

Negative correlations in temperature variations measured in the endwalls therefore corre-

spond to positive correlations in local vertical heat transport. As a control case, temperature correlations are calculated for thermistor pairs with both vertical and lateral separation. Discussed in detail in the appendix, these horizontally separated temperature correlations produce significantly less coherent behavior than the purely vertically separated pairs for quasi-geostrophic convection, in support of the interpretation of heat transfer by roughly vertical CTCs. This interpretation is further supported by a simple heat transfer model presented in section IV.

Correlation data for weakly rotating and non-rotating convection are shown in figure 4 **c** and **d**. Both cases have $R_f = 1.1 \times 10^{11}$. The case shown in panel c has $E = 3 \times 10^{-5}$, and the data in panel d come from a non-rotating convection experiment. Temperature correlations in the absence of dominant rotation (panels c and d) produce different thermal signatures from quasi-geostrophic convection (panel a and b). We observe broader, slightly positive correlation patterns in weakly and non-rotating convection experiments. This thermal signature is likely due to the development of large scale circulations as the influence of rotation wanes.

Large scale circulations have been found to produce positive thermal correlations in vertical thermistor pairs in non-rotating RBC experiments [e.g., 10]. In contrast to heat transport by CTCs, large scale circulations will typically produce vertically anti-correlated vertical heat flux, and therefore positively correlated temperature signals within the boundaries. In other words, the thermal boundary layers are thickest where the large scale circulation departs from the boundary (top left and bottom right corners of the cell depicted in figure1b), and thinnest where it impinges (top right and bottom left). The right half of a counterclockwise large scale circulation is anomalously warm, and the left half cold, and so produces positive vertical correlations and negative horizontal correlations [e.g., 28].

We may therefore interpret positively correlated thermal signals as evidence for the development of large scale circulations. In fact, visualizations in an uninsulated, non-rotating experiment with identical parameters as that shown in figure 4d confirm the existence of an large scale circulation. The detailed dynamics of large scale circulations are discussed elsewhere [e.g., 8, 11, 12], and so we will not focus on this flow regime here. The inferred presence of these strongly three-dimensional flow patterns, however, indicates the breakdown of quasi-geostrophic flow.

We should also note that the normalization used to calculate these correlations (2) inher-

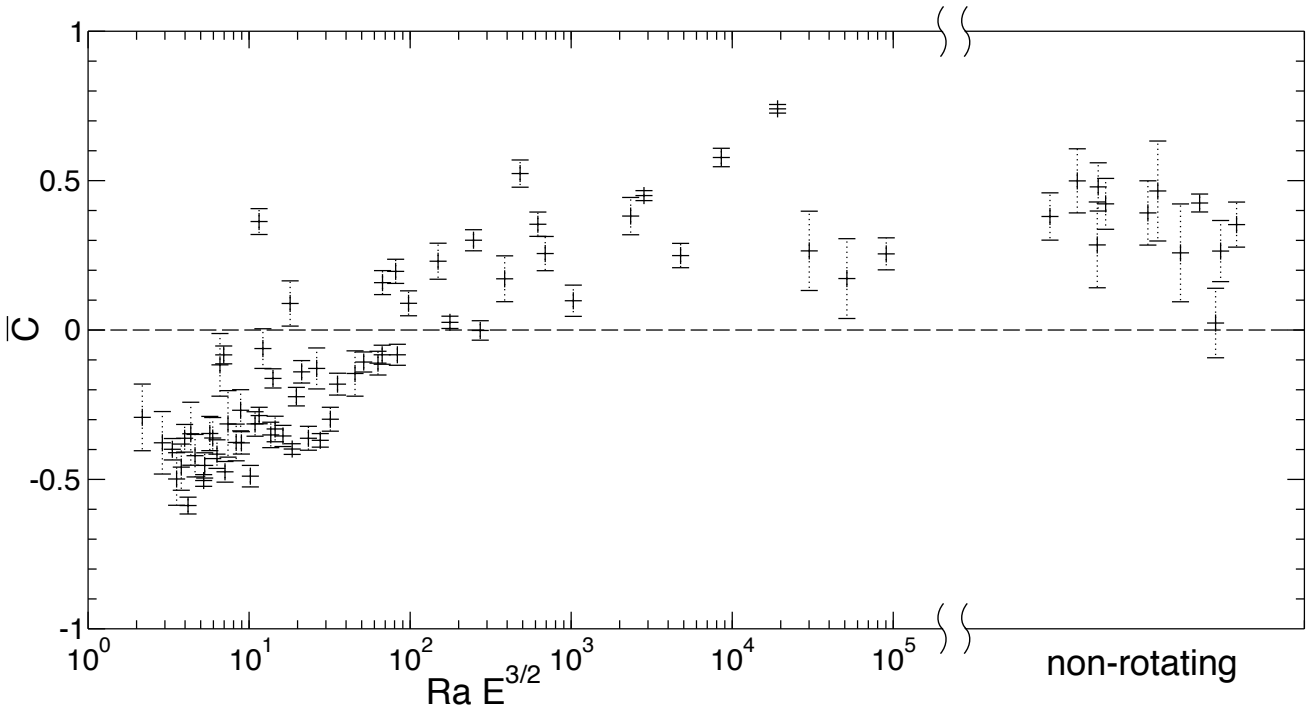

FIG. 5: Vertical temperature correlation coefficient at time lag m=0 ($\overline{C}$) as defined in (2), versus $RaE^{3/2}$. Errorbars represent one standard deviation among the six thermistor pairs for each case. Rightmost data are from non-rotating experiments, for which the x-coordinate is arbitrary.

ently assumes that the different thermistors sample all parts of the large scale circulation equally as the large scale circulation wanders azimuthally [e.g., 11]. If, however, the duration of experimental data acquisition were to be shorter than the timescale over which the large scale circulation wanders, or if the large scale circulation were to become locked in place, the cross-correlation should be normalized not by each thermistor's time-averaged temperature, but by the average of all thermistors on that level. Otherwise, we may be correlating small-scale plume behavior, instead of global dynamics. We have tried both normalizations, and find no appreciable change, indicating that we do, in fact, sample the large scale circulation without such azimuthal bias.

In figure 5, we show the mean zero-lag vertical temperature correlation coefficient $\overline{C}$ for all experiments. These data are plotted against the transition parameter $RaE^{3/2}$, which is argued to separate quasi-geostrophic and weakly rotating heat transfer regimes. In general, we observe anti-correlated signals in the quasi-geostrophic regime (small $RaE^{3/2}$), and

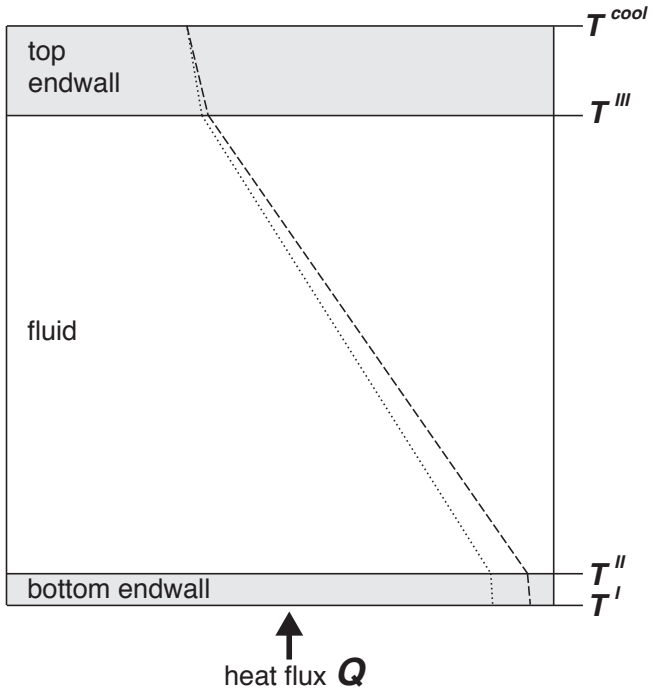

FIG. 6: A schematic illustration of the 1-Dimensional CTC heat transfer model. The three vertical layers, from bottom to top, are the bottom endwall, fluid layer, and top endwall. The vertical locations of the interfacial temperatures calculated in the model are denoted T^{I}, T^{II}, and T^{III}. The dotted and dashed lines illustrate instantaneous vertical temperature profiles generated by the model. The temperature gradient within the fluid layer varies with $Nu(t)$.

positively correlated signals in weakly (large $RaE^{3/2}$) and non-rotating ($E \approx \infty$) regimes. Negative correlations ($\overline{C} < 1$) are indicative of the importance of CTCs in transporting heat. Positive correlations ($\overline{C} > 1$) indicate the development of large scale circulations.

IV. 1-DIMENSIONAL CTC HEAT TRANSFER MODEL

In order to better understand the physical meaning of $C_i^{\mathrm{top-bottom}}$ in quasi-geostrophic convection experiments, we examine a simple one-dimensional numerical model for vertical heat transport by CTCs. The model consists of a vertical profile of a fluid layer sandwiched between two endwalls of finite thickness and thermal conductivity. As in the laboratory experiments, the temperature is fixed above the top endwall, and a heat flux is fixed below

the bottom endwall. We model the drifting CTCs as a region of temporally fluctuating yet vertically uniform heat flux. This is accomplished by characterizing the convecting fluid as a solid thermal conductor with an effective conductivity $k_{\text{eff}} = k_{\text{fluid}} Nu(t)$. Quantities used are accurate to material properties and experimental settings, and $Nu(t)$ is generated artificially. We calculate the vertical temperature profile of the model at each time step, generating synthetic temperature time series within the model's top and bottom boundaries. The correlation coefficient can then be calculated as in the actual experiment. This simple model provides synthetic data for an end-member convection scenario wherein heat is transferred entirely by space-filling, perfectly vertical CTCs. A more detailed description of the model is given below.

A. Model Details

First, a one dimensional model convection tank setup is constructed with dimensions to match the experiment, as shown in figure 6. The model consists of three layers (from bottom to top): a bottom endwall, which has thickness and thermal conductivity $h_{\text{bottom}} = 0.015$ m and $k_{\text{bottom}} = 390$ W/mK; a fluid layer with 'tank' height h_{fluid} and $k_{\text{fluid}} = 0.6$W/mK; and a top endwall with $h_{\text{top}} = 0.06$ m and $k_{\text{top}} = 167$ W/mK. The thermal boundary conditions are fixed heat flux below the bottom tank endwall, $q = Q/A$, where A is the area through which the heat power Q is fluxed, and fixed temperature above the top endwall, T^{cool}.

The basic idea of the model is to vary the efficiency of heat transfer in the fluid layer with time and solve for the temperature profile at each time step, t_i. We assume the convective heat transfer within the fluid is uniform in height, z, to approximate the behavior of an ideal CTC. This allows treatment of the fluid as a uniform material with effective thermal conductivity $k_{\text{eff}} = k_{\text{fluid}} Nu(t)$, where Nu is the Nusselt number. We use a time varying Nu to simulate a location in a three dimensional fluid layer through which Taylor columns pass as they wander horizontally around the container.

Time series for Nu are synthesized using a modified random walk. Initially, $Nu(t = 0) =$

Nu_0. For the remaining time steps $t_i = t_1, ..., t_{\max}$, we generate $Nu(t_i) = Nu_i$ as follows:

$$Nu_i = Nu_{i-1} + C_1(R_1^i - 1/2) \qquad \text{if } Nu_{i-1} = Nu_0; \quad (4)$$

$$Nu_i = Nu_{i-1} + C_1(R_1^i - 1/2) - C_2 R_2^i \; exp(-(Nu_0 - Nu_{i-1})/Nu_0) \qquad \text{if } Nu_{i-1} > Nu_0; \quad (5)$$

$$Nu_i = Nu_{i-1} + C_1(R_1^i - 1/2) + C_2 R_2^i \; exp((Nu_0 - Nu_{i-1})/Nu_0) \qquad \text{if } Nu_{i-1} < Nu_0; \quad (6)$$

where C_1 and C_2 are constants, and R_1^i and R_2^i are numbers in the range $0 < R < 1$ generated randomly at each time step. The constant C_1 determines the typical variability of Nu between time steps $(Nu_i - Nu_{i-1})$. The third term in (5) and (6) prescribes an exponentially weighted preference for Nu values to change in the direction of Nu_0. The constants C_1 and C_2 are positive and small, $0 < C < 1$, and are chosen such that the Nu time series is trendless about the desired value (Nu_0), and has statistical properties (e.g., variance, temporal power spectrum) similar to the actual experimental time series.

The temporal resolution of the model is set to match that of the acquisition frequency of experimental thermal measurements. We assume that the thermal diffusion timescale through the solid container boundaries is small compared to the typical time scale of fluctuations in convective heat transport. This assumption of instantaneous thermal equilibration allows us to solve for a thermally equilibrated temperature profile $T(z, t_i)$ at each time step. Based on visual observation of flow in non-rotating convection, and estimates of convective free fall, advective timescales are expected to be tens of seconds to minutes in our experiments. The timescale for thermal diffusion over distance d is $\tau_\kappa \sim d^2\kappa$, where κ is the material's thermal diffusivity. Copper and aluminum have $\kappa = 1.1 \times 10^{-4}$ and $\kappa = 6.4 \times 10^{-5}$, respectively [29]. The time scale for diffusion between the fluid layer and thermistors is approximately 0.05 s, which is faster than both advective time scales and acquisition frequency. The timescale for diffusion across the entire top and bottom endwalls is roughly 25 s and 1.5 s, respectively. The diffusive time scale through the upper endwall, therefore, is not significantly faster than advective timescales. A more advanced model could include the influence of finite thermal diffusivity, but, since we've already drastically reduced the complexity of the true system with this toy model, we anticipate that this additional effect will not alter its fundamental result. Experimental and numerical examinations of the effects of finite conductivity boundaries are given in [30, 31]

The heat flux and effective thermal conductivity are uniform in space within each layer, so the temperature will vary linearly in z within each layer, such that we need only solve

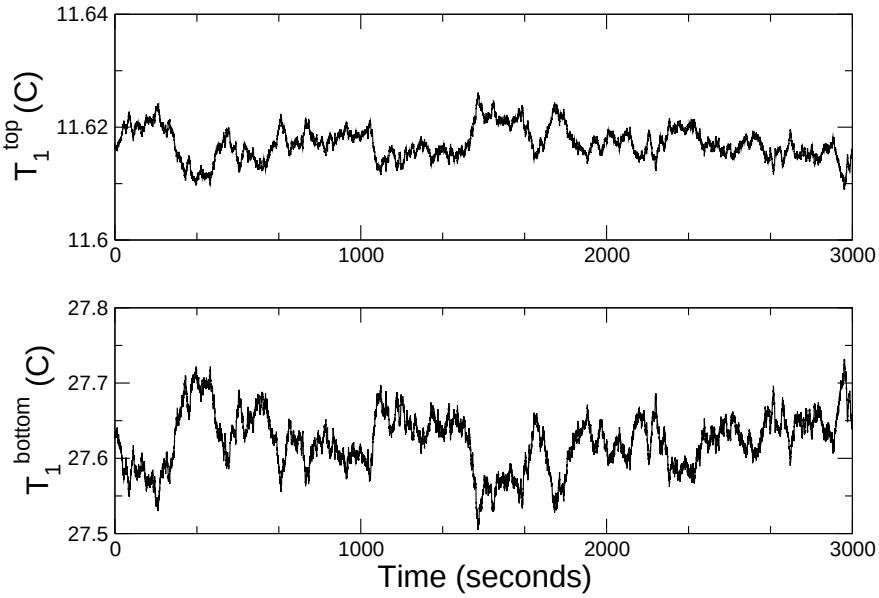

FIG. 7: An example of synthesized temperature time series data produced by the 1-D CTC heat transfer model. The top panel shows synthetic measurements in the top endwall ($T_1^{\rm top}(t)$), and the bottom panel shows data from the lower endwall ($T_1^{\rm bottom}(t)$). Model parameters are: $h_{\rm fluid} = 0.197$ m; $Q = 100$ W; $T^{\rm cool} = 10$ C; and $Nu_0 = 66$. Compare with experimental data shown in figure 3.

for the temperatures at the interfaces between layers. The temperature above the top endwall is fixed at $T^{\rm cool}$. The temperature between the top endwall and fluid is $T^{III}(t_i)$. The temperature between the fluid and the bottom endwall is $T^{II}(t_i)$. The temperature at the bottom of the lower endwall is $T^{I}(t_i)$. The locations of these interfacial temperature calculations, T^{I-III}, are shown in schematic figure 6. The aim of the model is to solve for these three temperatures at each time step t_i which depend on the predefined $Nu(t_i)$.

Initially, we take

$$T^{III}(t=0) = T^{\rm cool} + \frac{q\,h_{\rm top}}{k_{\rm top}} \tag{7}$$

$$T^{II}(t=0) = T^{III} + \frac{q\,h_{\rm fluid}}{Nu(t=0)\,k_{\rm fluid}} \tag{8}$$

$$T^{I}(t=0) = T^{II} + \frac{q\,h_{\rm bottom}}{k_{\rm bottom}}. \tag{9}$$

For the remainder of the time steps, $t_1, ..., t_{\max}$, the temperatures are solved for as

$$T^{III}(t_i) = T^{\text{cool}} + \frac{Nu(t_i)\, q\, h_{\text{top}}}{\langle Nu \rangle\, k_{\text{top}}} \tag{10}$$

$$T^{II}(t_i) = T^{III} + \frac{q\, h_{\text{fluid}}}{Nu(t_i)\, k_{\text{fluid}}} \tag{11}$$

$$T^{I}(t_i) = T^{II} + \frac{q\, h_{\text{bottom}}}{k_{\text{bottom}}}. \tag{12}$$

Notice that the temperature above the fluid, $T^{III}(t_i)$, is dependent on fluctuations of Nu about it's mean $\langle Nu \rangle \approx Nu_0$. This is due to the convecting fluid's control of how much of the base heating q reaches the top endwall, as the fluid acts as a heat flux capacitor.

Once the temperature profile time series are generated, it is possible to extract a synthetic thermistor time series measurement. In the experiment, the thermistors are located within the endwalls, 2 mm from the fluid boundary. Synthetic top and bottom thermistor data are then

$$T^{\text{top}}(t_i) = T^{III}(t_i) - \left(\frac{0.002\,\text{m}}{h_{\text{top}}}\right)(T^{III}(t_i) - T^{\text{cool}}) \tag{13}$$

$$T^{\text{bottom}}(t_i) = T^{II}(t_i) + \left(\frac{0.002\,\text{m}}{h_{\text{bottom}}}\right)(T^{II}(t_i) - T^{II}(t_i)). \tag{14}$$

Examples of these synthetic thermistor data are shown in figure 7, and can be compared directly to experimental data (figure 3). Note that the top temperature shows much smaller variance than both the bottom temperature, as well as the top temperature from actual experiments. This is likely due to the assumption of instantaneous thermal equilibration, which will smooth vertical variations and limit their amplitude. The absolute amplitude of variations, however, are not important for normalized cross-correlation coefficients, which are calculated for the synthetic data exactly as in actual experiments using (2).

B. Model Results

Figure 8 shows calculations of vertical correlations, $C_i^{\text{top-bottom}}$, from six model iterations. The model parameters are set to $h_{\text{bottom}} = 0.015$ m, $k_{\text{bottom}} = 390$ W/mK, $h_{\text{fluid}} = 0.197$ m, $k_{\text{fluid}} = 0.6$W/mK, $h_{\text{top}} = 0.06$ m, $k_{\text{top}} = 167$ W/mK, $Q = 100$ W, $T^{\text{cool}} = 10$ C, $t_{\max} = 3000$ s, $Nu_0 = 66$, $C_1 = 0.01$, and $C_2 = 0.0004$. These values are chosen in order to simulate the experimental setting from which the data in figures 3 and 4a are collected.

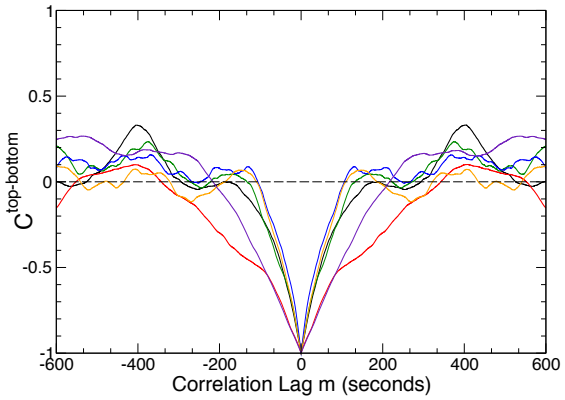

FIG. 8: Temperature correlations calculated from synthetic thermistor data from the 1-D CTC heat transfer model. Model parameters are $h_{\text{fluid}} = 0.197$ m, $Q = 100$ W, $T^{\text{cool}} = 10$ C, and $Nu_0 = 66$. Six separate model results are shown, wherein different Nu time series are used in order to approximate the six different thermistor pairs used in actual experiments. Instantaneous temperature values within the top and bottom endwalls are strongly anti-correlated.

At zero time lag (m = 0), the correlation is perfect ($|\overline{C}| = 1$), owing to the assumption of perfectly uniform, vertical heat transport at each time step. The sign of the correlation, however, is negative, in agreement with the thermal anti-correlations observed experimentally (figure 4a & b)

The nature of the time series used for $Nu(t)$ is unimportant for producing anti-correlated temperature calculations at zero lag. If $Nu(t)$ varies as white noise, for example, we again find a perfect anti-correlation at $m = 0$. But, since each value in a white time series is independent of the previous value, $C(m \neq 0) = 0$ over an ensemble average. In order to produce correlation profiles with broader ranges of non-zero values, the time series must have non-zero autocorrelation. The width of the troughs observed in figures 4 (a & b) and 8 are therefore linked to the spectral properties of the time series, which is in turn linked to the convective flow. We leave a detailed analysis of temporal spectra for future work.

V. DISCUSSION

Figures 1c and 4b both show results from rapidly rotating, turbulent Rayleigh-Bénard convection with $R_f = 1.1 \times 10^{11}$ and $E = 3 \times 10^{-6}$. Figure 8 shows synthetic data from an idealized model of heat transport by Taylor columns with parameters set to simulate these experiments. The qualitative agreement between experimental correlation measurements and the synthetic model data supports the idea that anti-correlated temperature measurements are indicative of the presence of CTCs. That the model data have a much stronger anti-correlation is due to the assumption of perfectly uniform, perfectly vertical instantaneous heat transport at all times. Possible causes for imperfect correlation ($|\overline{C}| < 1$) in experiments include: lateral diffusion of heat in CTCs and endwalls; diffusive heat transport in the space between CTC cores; and CTCs may not be perfectly vertical and container-high. Flow visualizations (figures 1c), however, further verify the columnar nature of flow in experiments with identical parameters to those that produce vertically anti-correlated temperature signals (figure 4b). The general agreement between these three figures indicates that convection within this regime is manifest as tall, roughly vertical, thermally active CTCs.

Ref. [25] shows that the thermal boundary layer is thinner than the Ekman boundary layer when $RaE^{3/2} \gtrsim 20$ in rotating RBC simulations. This transition also corresponds to a change in heat transfer behavior from quasi-geostrophic to weakly rotating. Here, we observe that some experiments with $20 < RaE^{3/2} \lesssim 100$ produce anti-correlated signals. From this we infer that when the thermal boundary layer thickness is smaller than but comparable to the Ekman boundary layer thickness, CTCs can still exist. This contention is in agreement with the idea that the intensification of heat transfer observed near this transition is related to Ekman pumping in the presence of a thermal boundary layer [32]. The scatter in experimental $\overline{C}$ data precludes the identification of any clear transition point between quasi-geostrophic CTCs and weakly rotating large scale circulation. This difficulty remains regardless of the abscissa parameter chosen in figure 5 (including, for example, the convective Rossby number, $Ro_c = (RaE^2/Pr)^{1/2}$).

To summarize, we find two rotating convective regimes, termed quasi-geostrophic and weakly rotating. In quasigeostrophic convection, heat is transported by tall, thin, vertical conduits known as convective Taylor columns. These flow structures wander about hori-

zontally, pumping warm fluid from bottom to top or vice versa. Locally, this flow (nearly) simultaneously cools the bottom boundary and cools the top boundary due to their finite conductivity, and therefore produces anti-correlated vertical temperature signatures. In the weakly rotating regime, large scale circulations produce warm and cool 'piles' of material that generate positively correlated vertical temperature signatures.

It remains unclear over what range of parameters CTCs are stable. The width of a CTC should scale as $E^{1/3}$ [33]. As E decreases to the very low values predicted in planetary settings, CTCs become increasing thin, and may undergo instabilities [34]. Furthermore, in low Pr fluids such as liquid metals, the thermal anomalies carried in CTCs may be more effectively diffused, and so the columns may not extend across the layer. As an example, the observation of two pairs of geomagnetic flux patches that are nearly symmetric about the equator evoke, as an explanation, the existence of CTCs in Earth's field-generating core [e.g., 35, 36]. Earth's liquid metal outer core has $E \approx 10^{-15}$ and $Pr \lesssim 0.1$, and it is not clear that large scale CTCs can exist in such an extreme setting. We can answer these questions by looking for evidence of CTCs in experiments with increasingly extreme parameters.

Acknowledgements

EMK acknowledges the support of the Miller Institute for Basic Research in Science. JMA was funded by the NSF Geophysics Program (EAR-0944312) and the NASA Planetary Atmospheres Program (NNX09AB61G).

---

[1] G. I. Taylor, Proceedings of the Royal Society of London Series A **100**, 114 (1921).

[2] K. Julien and E. Knobloch, Physics of Fluids **11**, 1469 (1999).

[3] G. Veronis, Journal of Fluid Mechanics **5**, 401 (1959).

[4] M. Sprague, K. Julien, E. Knobloch, and J. Werne, Journal of Fluid Mechanics **551**, 141 (2006).

[5] J. McWilliams, *Fundamentals of Geophysical Fluid Dynamics* (Cambridge University Press, 2006).

[6] S. Sakai, Journal of Fluid Mechanics **333**, 85 (1997).

[7] E. King, S. Stellmach, J. Noir, U. Hansen, and J. Aurnou, Nature **457**, 301 (2009).

[8] J. Hart, S. Kittelman, and D. Ohlsen, Physics of Fluids **14**, 995 (2002).

[9] J.-Q. Zhong and G. Ahlers, Journal of Fluid Mechanics **665**, 300 (2010).

[10] S. Cioni, S. Ciliberto, and J. Sommeria, Journal of Fluid Mechanics **335**, 111 (1997).

[11] E. Brown and G. Ahlers, Physical Review Letters **98**, 134501 (2007).

[12] H. Xi, S. Lam, and K. Xia, Journal of Fluid Mechanics **503**, 47 (2004).

[13] H. Rossby, Journal of Fluid Mechanics **36**, 309 (1969).

[14] K. Julien, S. Legg, J. McWilliams, and J. Werne, Journal of Fluid Mechanics **322**, 243 (1996).

[15] Y. Liu and R. Ecke, Physical Review Letters **79**, 2257 (1997).

[16] J. Aurnou, Geophysical and Astrophysical Fluid Dynamics **101**, 327 (2007).

[17] Y. Liu and R. Ecke, Physical Review E **80**, 6314 (2009).

[18] J. Zhong, R. Stevens, and H. Clercx, Physical Review Letters **102**, 044502 (2009).

[19] E. King, K. Soderlund, U. R. Christensen, J. Wicht, and J. M. Aurnou, Geochemistry Geophysics Geosystems **11**, Q06016 (2010).

[20] J. J. Niemela, S. Babuin, and K. R. Sreenivasan, Journal of Fluid Mechanics **649**, 509 (2010).

[21] S. Schmitz and A. Tilgner, Physical Review E **80**, 5305 (2009).

[22] S. Schmitz and A. Tilgner, Geophysical and Astrophysical Fluid Dynamics pp. 1–8 (2010).

[23] B. Boubnov and G. Golitsyn, Journal of Fluid Mechanics **219**, 215 (1990).

[24] E. M. King, Ph.D. thesis, University of California, Los Angeles (2009).

[25] E. M. King, S. Stellmach, and J. M. Aurnou, Journal of Fluid Mechanics (2011, in review).

[26] J. Noir, D. Brito, K. Aldridge, and P. Cardin, Geophysical Research Letters **28**, 3785 (2001).

[27] D. Hathaway, Astrophysical Journal **276**, 316 (1984).

[28] J. J. Niemela and K. R. Sreenivasan, Journal of Fluid Mechanics **557**, 411 (2006).

[29] D. R. Lide, *Handbook of Chemistry and Physics* (CRC Press, 2000).

[30] E. Brown, A. Nikolaenko, D. Funfschilling, and G. Ahlers, Physics of Fluids **17**, 075108 (2005).

[31] R. Verzicco, Physics of Fluids **16**, 1965 (2004).

[32] R. J. A. M. Stevens, H. J. H. Clercx, and D. Lohse, Physics of Fluids **22**, 085103 (2010).

[33] S. Chandrasekhar, *Hydrodynamic and Hydromagnetic Stability* (Dover Publications, 1961).

[34] P. Billant, Journal of Fluid Mechanics **660**, 354 (2010).

[35] D. Gubbins and J. Bloxham, Nature **325**, 509 (1987).

[36] P. Olson, U. Christensen, and G. Glatzmaier, Journal of Geophysical Research **104**, 10383 (1999).

Appendix

To serve as a control group for the conclusions drawn from the correlation data shown in figure 4, we have calculated correlations between thermistor pairs with both vertical and lateral separation. We look at correlations with two types of lateral separation: either azimuthal neighbors (minimally offset), with 7 cm lateral separation; or maximally separated diametrically opposed pairs (antipodal), separated by 13 cm laterally. For quasi-geostrophic experiments, some of these pairs do still produce negative correlations, but these are always weaker than the correlations between purely vertical thermistors, and grow weaker with increasing lateral separation.

Figure 9 shows a comparison of correlation coefficients for six types of thermistor pairs: a) autocorrelation of the thermistor signal with itself; b) horizontal pairs of nearest neighbors; c) horizontal pairs of diametrically opposed thermistors; d) vertically aligned and vertically separated thermistors (our original analysis); e) minimally laterally offset and vertically separated thermistors; and f) maximally laterally separated and vertically separated (antipodal) pairs. The experimental case shown is the same as in figure 4a, which is in the geostrophic regime ($RaE^{3/2} \approx 5$). These geostrophic correlations become less coherent as lateral separation is increased.

Figure 10 shows a comparison of correlation coefficients for the six types of thermistor pairs, as shown in figure 9, but now for the weakly rotating convection experiment data shown in figure 4c. The correlations are weak in general. We do notice that the weak positive correlations seen in the purely vertically separated pair are complemented by weakly anti-correlated signals for the antipodal pairs. This fits with our interpretation of these thermal signatures as being produced by large scale circulations, which should produce heat flux anomalies that are anomalously high in the tank corners that are antipodally opposed.

We can test the CTC interpretation of the temperature correlations more systematically by determining the time lag at which vertical correlations are maximally anti-correlated in the geostrophic experiments. Heat transfer by wandering CTCs should result in maximum anti-correlations at lag ($k \approx 0$) for the vertically aligned thermistor pairs, but should show no strong bias in lag-space for the horizontally separated pairs. We calculate the lag at which the correlation coefficient is minimal (within a ten minute lag range) for each pair for the 64 cases with $RaE^{3/2} < 10$. Figure 3 shows a histogram of the results of this calculation.

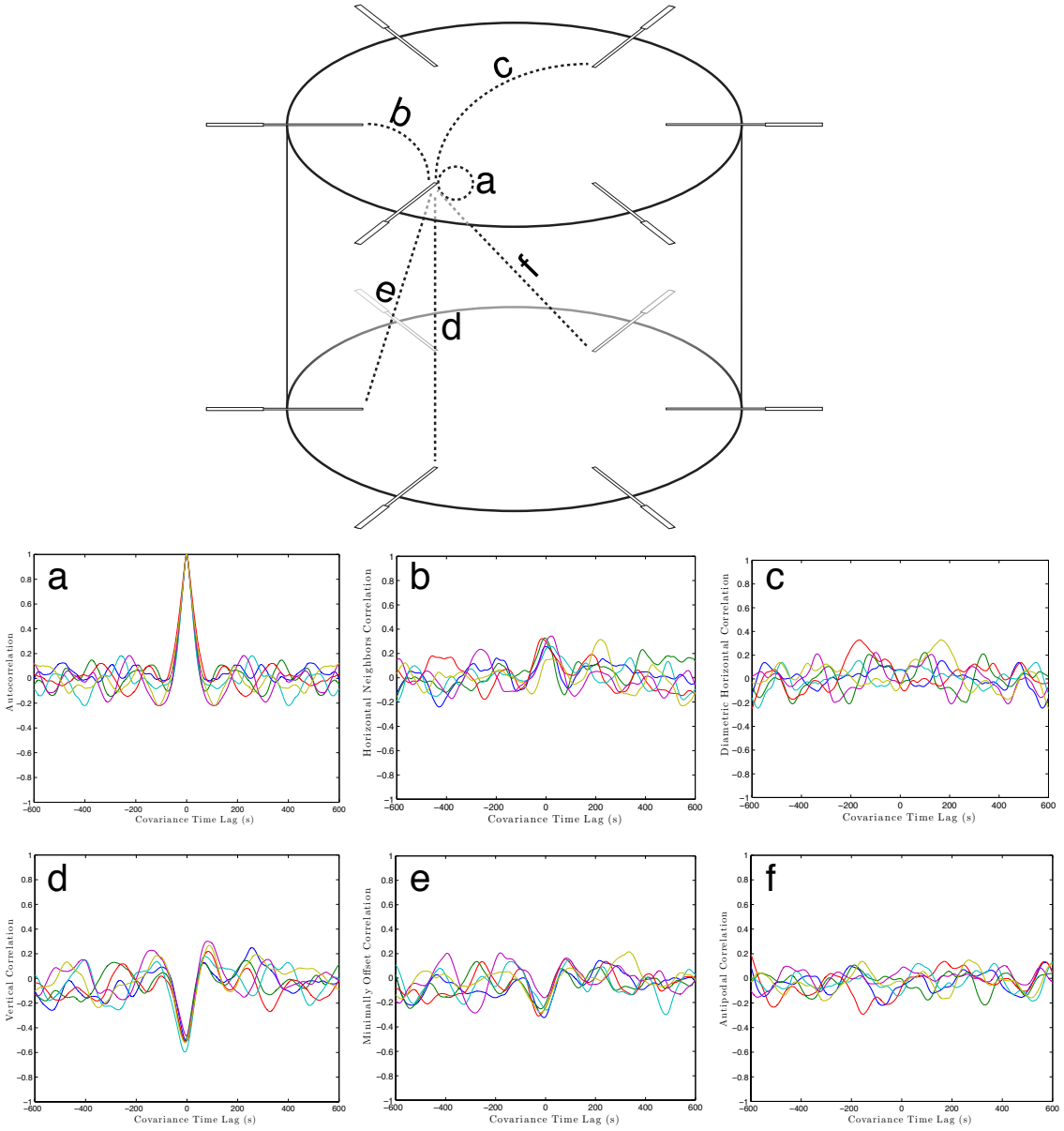

FIG. 9: Temperature correlations from a geostrophic convection experiment plotted versus correlation lag for six types of thermistor pairs: a) autocorrelation of the thermistor signal with itself; b) horizontal pairs of nearest neighbors; c) horizontal pairs of diametrically opposed thermistors; d) vertically aligned and vertically separated thermistors (our original analysis); e) minimally laterally offset and vertically separated thermistors; and f) maximally laterally separated and vertically separated (antipodal) pairs. The experimental case shown has $h = 4.7$ cm, $Q = 50$ W, and $\Omega = 5.3$ Hz, and therefore $R_f = 2 \times 10^8$, $E = 4.4 \times 10^{-5}$, $RaE^{3/2} \approx 5$. Panel d) is identical to figure 4a.

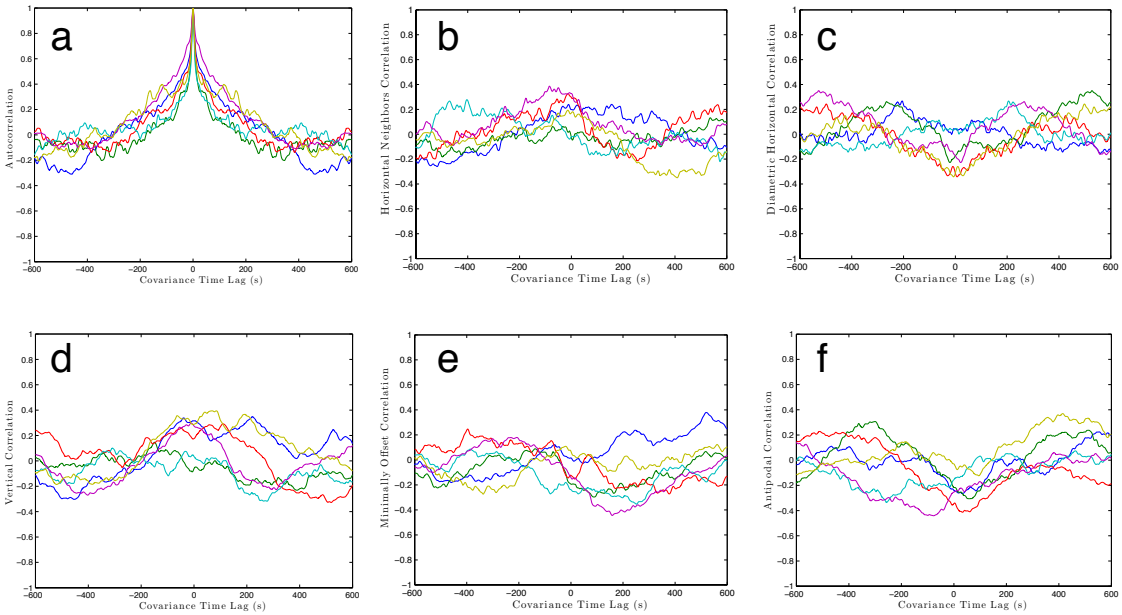

FIG. 10: Vertically and/or horizontally separated temperature correlations from a weakly rotating convection experiment plotted versus correlation lag. As in figure 9, the six types of thermistor pairs are: a) autocorrelation of the thermistor signal with itself; b) horizontal pairs of nearest neighbors; c) horizontal pairs of diametrically opposed thermistors; d) vertically aligned and vertically separated thermistors (our original analysis); e) minimally laterally offset and vertically separated thermistors; and f) maximally laterally separated and vertically separated (antipodal) pairs. The experimental case shown has $h = 19.7$ cm, $Q = 100$ W, and $\Omega = 0.43$ Hz, and therefore $R_f = 1 \times 10^{11}$, $E = 3 \times 10^{-5}$, $RaE^{3/2} \approx 280$. Panel d) is identical to figure 4c.

For the pairs with purely vertical separation (a), there is a strong likelihood that geostrophic convection will produce minimum correlation (maximum anti-correlation) near $k = 0$. For pairs with lateral separation (b & c), this strong preference disappears. This supports our argument that the anti-correlations observed in vertical pairs for geostrophic convection are due to wandering Taylor columns.

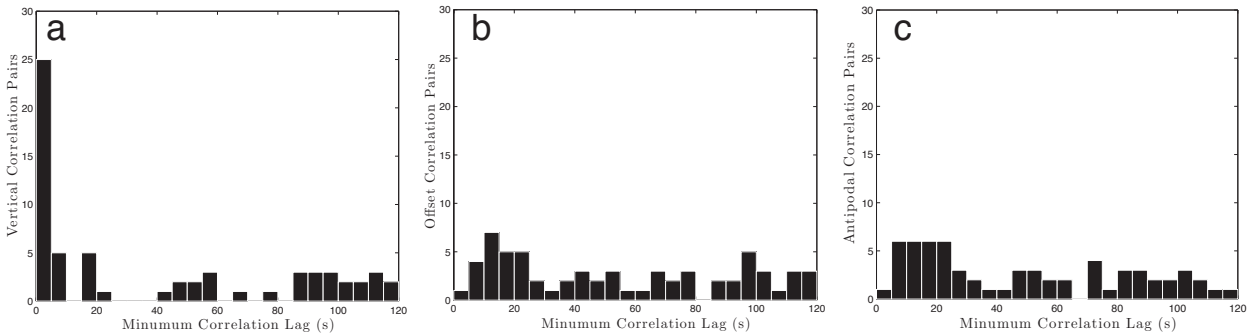

FIG. 11: Histograms of the time lags at which vertically separated thermistor pairs produce maximum anti-correlations for geostrophic experiments ($RaE^{3/2} < 10$). Panel a shows data from thermistor pairs with no lateral separation. Panel b shows data from minimally laterally offset pairs. Panel c shows antipodal (maximally offset) pairs.